PAPER

Check for updates

Rational design of Au@Pd core–shell cocatalyst on titanium dioxide enabling selective photocatalytic formation of deuterated alkane from lauric acid and heavy water

Haifan Huang and Hisao Yoshida [iD] *

Photocatalytic decarboxylative deuteration using heavy water is a promising approach for the synthesis of deuterated alkane, where high reaction selectivity is essential. In this study, Au@Pd-loaded TiO$_2$ photocatalysts are prepared *via* a simultaneous photodeposition (SPD) method under various conditions, and the effects of the preparation conditions on cocatalyst structure, as well as the resulting photocatalytic activity and selectivity toward deuterated undecane formation from lauric acid and heavy water, are systematically investigated. In the SPD process, efficient reduction of the metal precursors with a higher density of the photoexcited electrons, which can be provided by high light intensity or efficient sacrificial reagents such as methanol, leads to the formation of Au@Pd core–shell nanoparticles covered with a Pd-rich shell surface, resulting in a high yield and selectivity for deuterated undecane. The Au@Pd core–shell part has concentration gradient of Au and Pd to accelerate smooth migration from the Au core to the Pd-rich surface after receiving the photoexcited electron from TiO$_2$ surface, enhancing the photocatalytic activity due to high electron density at the Pd surface, and the Pd-rich surface consists of almost pure Pd, promoting the deuterium ion reduction to deuterium radical and successive reaction between the generated deuterium radical and undecyl radical generated by hole oxidation on the TiO$_2$ surface. This acceleration contributes to the high selectivity for the deuteration. These results demonstrate that rational control of photodeposition parameters to fabricate the well-designed functional cocatalyst is a promising strategy to obtain high photocatalytic activity and reaction selectivity in the photocatalytic synthesis of deuterated alkane.

Introduction

Deuterium-labeled compounds play a crucial role in modern science and industry due to their wide-ranging applications in pharmaceuticals,[1–3] metabolic tracing,[4,5] kinetic isotope effect studies,[6] and materials chemistry.[7] From an application perspective, the approval of the deuterated drug, deutetrabenazine by the U.S. FDA in 2017 highlights the practical value of deuteration technology.[8,9] Therefore, the development of efficient and sustainable deuteration methods remains of great significance.

Various deuteration strategies have been developed to incorporate deuterium (D) into organic molecules. Among them, the most widely used is hydrogen isotope exchange (HIE) using D$_2$ gas, which allows direct substitution of H atoms with D in existing compounds without extensive pre-functionalization.[10–13] Other approaches include reductive

deuteration,[14] where deuterium sources such as D$_2$O or CD$_3$OD are used in the presence of hydrogenation catalysts to install C–D bonds. Radical deuteration methods[15] have also emerged recently; these utilize radical pathways to effect D-incorporation under milder conditions with high functional-group tolerance. However, many of these strategies still require costly deuterium sources (*e.g.*, D$_2$ gas)[16–19] and harsh conditions,[20–24] limiting their sustainability and broad applicability.
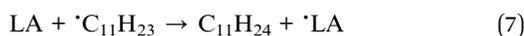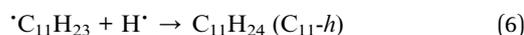
Recent studies have reported remarkable progress in the synthesis of bimetallic nanomaterials,[25–27] particularly in the precise control of Au and Pd atomic distributions.[28] Among them, Au-core/Pd-shell nanostructures have attracted considerable attention due to their ability to synergistically enhance both catalytic activity and selectivity. For example, Hoeven[29] reported an Au–Pd core–shell nanorods reveal higher catalytic activity than their alloy counterparts in the selective hydrogenation of butadiene with high selectivity. Some studies also demonstrated that Au–Pd core–shell catalysts exhibit superior performance compared to their monometallic or alloy counterparts in the selective oxidation of benzyl alcohol.[30,31] This enhancement arises from the unique electronic and geometric

Graduate School of Human and Environmental Studies, Kyoto University, Yoshida-nihonmatsu-cho, Sakyo-ku, Kyoto 606-8501, Japan. E-mail: yoshida.hisao. 2a@kyoto-u.ac.jp

interactions between the Au core and Pd shell, which effectively modulate surface reactivity.

In our previous studies, we demonstrated that a TiO_2 photocatalyst with a metal cocatalyst promotes photocatalytic decarboxylative deuteration using lauric acid (LA) and heavy water (eqn (1))[32] and the use of a bimetallic cocatalyst composed of a Au core and Pd shell (Au@Pd/TiO_2) exhibited higher yield and selectivity compared to monometallic counterparts.[33] The reaction starts with photocatalytic hole oxidation of LA to form undecyl radical, $^{\bullet}C_{11}H_{23}$ (eqn (2)). Photoexcited electron reduces deuterium ion (D^+) to form deuterium radical ($D^{\bullet}$) (eqn (3) and (4)). The undecyl radical can react in three pathways as follows; (i) reaction with $D^{\bullet}$ to produce deuterated alkane, C_{11}-d (as the aimed product, eqn (5)), (ii) reaction with $H^{\bullet}$ or LA to give undeuterated alkane, C_{11}-h (a hard-to-remove byproduct, eqn (6) and (7)), and (iii) reaction with another undecyl radical to form docosane, C_{22} (a byproduct, eqn (8)).[33] The enhanced performance of the bimetallic cocatalyst arises from the complementary roles of the two elements of the core–shell cocatalyst: the Au core contributes to efficiently accepting the photoexcited electrons from TiO_2 and passing them to the Pd shell, and the Pd shell contributes to the generation of $D^{\bullet}$ radical and the successive coupling with the undecyl radical, $^{\bullet}C_{11}H_{23}$. As a result, the Au@Pd core–shell structure realize high selectivity.

$$C_{11}H_{23}COOH + D_2O \rightarrow C_{11}H_{23}D + CO_2 + HDO \quad (1)$$

$$C_{11}H_{23}COOH + h^+ \rightarrow {}^{\bullet}C_{11}H_{23} + CO_2 + H^+ \quad (2)$$

$$D_2O \rightarrow D^+ + OD^- \quad (3)$$

$$D^+ + e^- \rightarrow D^{\bullet} \quad (4)$$

$${}^{\bullet}C_{11}H_{23} + D^{\bullet} \rightarrow C_{11}H_{23}D \ (C_{11}\text{-}d) \quad (5)$$

$${}^{\bullet}C_{11}H_{23} + H^{\bullet} \rightarrow C_{11}H_{24} \ (C_{11}\text{-}h) \quad (6)$$

$$LA + {}^{\bullet}C_{11}H_{23} \rightarrow C_{11}H_{24} + {}^{\bullet}LA \quad (7)$$

$$2{}^{\bullet}C_{11}H_{23} \rightarrow C_{22}H_{46} \ (C_{22}) \quad (8)$$

However, these beneficial effects are highly sensitive to preparation conditions such as the photodeposition light intensity and type of sacrificial reagent, which decide the resulting composition, morphology, and catalytic activity. In the present study, we aim to clarify how these preparation conditions influence the structure of Au@Pd cocatalyst and its consequent performance in photocatalytic decarboxylative deuteration of lauric acid with heavy water.

Results

Simultaneous and sequential preparation

Our previous study[33] reveals that the TiO_2 photocatalyst with a bimetal cocatalyst (1 wt% Au and 2 wt% Pd) prepared by the simultaneous photodeposition (SPD) method has core–shell Au@Pd metal nanoparticles and exhibits high performance in

photocatalytic synthesis of deuterated alkane from lauric acid and heavy water through decarboxylation. Here, photocatalytic reaction tests were conducted using various TiO_2 samples prepared by different preparation methods to load cocatalyst of the same loadings (1 wt% Au and 2 wt% Pd), and the results are presented in Fig. 1. The main products obtained in the liquid phase were deuterated n-undecane (C_{11}-d) as a target product and non-deuterated n-undecane (C_{11}-h) and n-docosane (C_{22}) as byproducts, whereas hydrogen (H_2 or D_2) and carbon dioxide (CO_2) were detected in the gas phase. Among the gas products, CO_2 is a product of the desired reaction (eqn (1)), while H_2 is likely generated through dehydrogenative reactions among organic molecules and D_2 should be formed *via* water splitting.

The sample prepared by the SPD, Au@Pd/TiO_2 (Fig. 1a) showed higher selectivity to C_{11}-d, which is shown as S_d and R_d values, than the sample prepared by the stepwise photodeposition, Pd2/Au1/TiO_2 and Au1/Pd2/TiO_2 (Fig. 1b and c),[33] highlighting the SPD is a superior method to fabricate sufficient cocatalyst than the stepwise photodeposition. Another sample prepared by a stepwise method combining chemical reduction (CR) and photodeposition (PD) methods, Pd2(PD)/Au1(CR)/TiO_2, exhibited a lower yield of C_{11}-d, Y_{C11}-d and a higher yield of C_{22}, Y_{C22} than Pd2/Au1/TiO_2, along with the lowest S_d and R_d among the four tested samples.

STEM-EDX mapping revealed partial overlap between Pd (green) and Au (red) signals of these samples. The images of the Au1@Pd2/TiO_2 sample (Fig. S1a–d) presented particles with an apparent Au-core/Pd-shell architecture (Au@Pd), where the Pd shell thickness was 1–1.5 nm and the mean particle size of NPs was 7.53 nm.[33] The boundary between core and shell was not sharp, suggesting partial incorporation of Pd into the Au core and Au into the Pd shell. This means that a concentration gradient of Pd and Au is present within the core–shell structure; the concentration of Pd gradually increases toward the surface
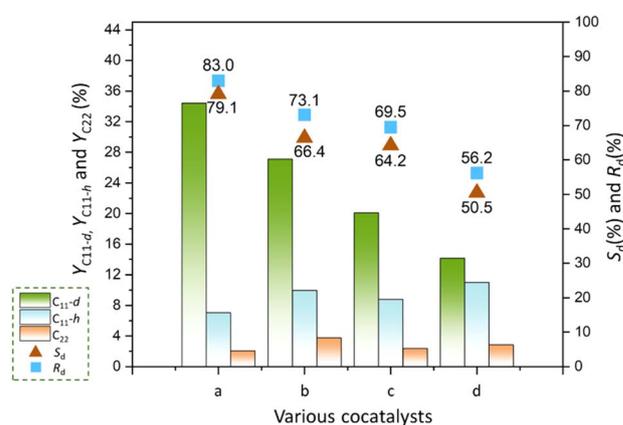

Fig. 1 Results of photocatalytic reaction tests with the photocatalyst samples containing 1 wt% Au and 2 wt% Pd cocatalysts with various cocatalysts; (a) Au1@Pd2/TiO_2, (b) Pd2/Au1/TiO_2, (c) Au1/Pd2/TiO_2, and (d) Pd2(PD)/Au1(CR)/TiO_2. The green, light blue, and orange bars represent Y_{C11}-d, Y_{C11}-h, and Y_{C22}, respectively. Dark red triangles indicate S_d (selectivity to C_{11}-d), and light blue squares show R_d (selectivity to C_{11}-d in the obtained undecanes). The reaction time was 3 h. Data are taken from Table S1; see the caption of Table S1 for other reaction conditions.

of the core–shell Au@Pd NPs, which is discussed later. A line-scan analysis was conducted as indicated by the inset of Fig. S2, and the corresponding results are presented as a bar chart (Fig. S2). The x-axis represents the distance across the line, while the y-axis shows the elemental signal intensity normalized with the atomic ratio. This quantitative profile clearly visualizes the elemental distribution within the Au@Pd core–shell structure. As shown, the Pd signal dominates at the outer regions of both sides, indicating that Pd is mainly enriched at the surface, whereas the Au content significantly increases toward the center of the particle. This result further confirms the formation of a distinct Au-core@Pd-shell configuration and provides quantitative evidence of the compositional gradient across the bimetallic nanoparticle.

In the SPD method, the copresence of Pd and Au precursors in the solution leads to concurrent adsorption and surface reductions by the photoexcited electrons, and competitive growth, favoring intermixing alloy formation and producing ambiguous core–shell interfaces with the concentration gradient. This specific structural property reflects differences in deposition kinetics of Au and Pd, i.e., competition of both the adsorption of the metal precursors and the surface photoreduction by the photoexcited electrons. Considering the standard reduction potentials of Au^{3+} and Pd^{2+}, +1.40 V and +0.915 V,[34,35] respectively and the result of the core–shell composition, the Au deposition should take place faster than the Pd deposition, as evidenced later. At the initial stage of the SPD process, Au predominantly deposited in the TiO_2 surface to generate the Au nuclei, followed by growing into larger cores with predominant addition of Au and increasing portion of Pd, resulting the production of larger core–shell Au@Pd NPs with a concentration gradient. In the case of the Au1@Pd2/TiO_2 sample, the ratio of Au and Pd were 0.4 and 1.5 atm.%, respectively. Since the amount of Au is relatively small and deposited faster, Au is photodeposited completely at an early stage, and subsequently only Pd is photodeposited, giving the shell consisting of pure Pd as confirmed later.

In contrast, the sequentially stepwise photodeposited Pd2/Au1/TiO_2 sample (Fig. S1e–h) exhibited a more distinct core–shell structure, in which the Pd shell is clearly estimated as 0.8–1.2 nm, and the average particle size increased to 18.2 nm. The opposite sequential stepwise PD gives Au1/Pd2/TiO_2, which showed no clear core–shell structures but random spatial distribution of Pd NPs (3–7 nm) and dispersed Au species (Fig. S1i–l). Since Pd has a relatively lower photoreduction rate than Au, the adsorbed Pd precursor would be slowly reduced during the adsorption–desorption equilibrium, resulting that highly dispersed small Pd nanoparticles formed on the TiO_2 surface. In the second step, since Au can be easily photodeposited, they are deposited not only on the surface of Pd NPs but also the exposed TiO_2 surface, resulting unclear small core–shell NPs.

The Pd2(PD)/Au1(CR)/TiO_2 sample did not show a clear core–shell structure; there are various kinds of particles (Fig. S1m–p). The first CR step cannot limit the deposition sites for Au NPs, in other words, Au NPs can be chemically formed anywhere on the TiO_2 surface, including reductive, oxidative, and even neutral sites, and occasionally very large NPs (40 nm) were also formed. In the second PD step, Pd species form NPs on the reduction sites, resulting in a variety of NPs.

As a conclusion of this section, the concentration gradient Au@Pd core–shell NPs prepared by the SPD method is confirmed to be suitable for this photocatalytic reaction. As discussed in the previous study,[33] the Au rich core efficiently receives the photoexcited electrons from the TiO_2 photocatalyst. The concentration gradient in the NP allows the migration of the electrons from the Au-rich core to the Pd-rich surface, providing high electron density at the Pd-rich shell and thus high reduction rate. The Pd-rich surface has a prominent property for the reduction of deuterium cation (D^+) to deuterium radical ($D^{\cdot}$) (eqn (4)) and the successive deuteration of the undecyl radical formed on the oxidative site on the TiO_2 surface (eqn (5)), contributing the high reaction selectivity.

Simultaneous photodeposition conditions

The photocatalytic reaction was carried out with several Au1@Pd2/TiO_2 photocatalysts that were prepared by the SPD method with various photoirradiation conditions, such as light intensities and irradiation time (Fig. 2). The higher $Y_{C11\text{-}d}$ was observed on the samples prepared with the higher light intensity in the SPD process, as increased from 9.5 to 76.2 mW cm^{-2} (Fig. 2a–d). In contrast, $Y_{C11\text{-}h}$ as a byproduct was not so changed with the SPD light intensity up to 38 mW cm^{-2} and decreased when it was 76.2 mW cm^{-2}, resulting in the highest S_d for the sample prepared by the highest light intensity. Among these samples, an obvious color change was observed from dark grey to deep purple with the decrease of light intensity (Fig. S4), indicating that the SPD light intensity can vary the state of cocatalyst.

Table 1 shows the actual loading amount of Au and Pd in these samples. The loading amount of the Au1@Pd2/TiO_2 sample prepared with the highest SPD light intensity (76.2 mW cm^{-2}) was confirmed to be the intended values, 1 wt% Au and
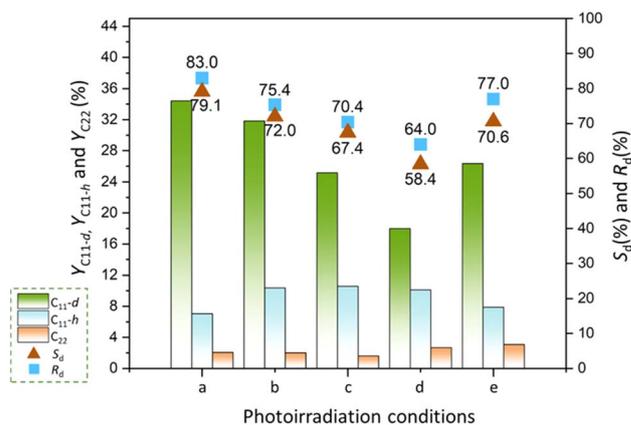

Fig. 2 Results of photocatalytic reaction tests with the Au1@Pd2/TiO_2 samples prepared by the SPD method with different photoirradiation conditions. Photoirradiation was carried out with the various light intensity such as (a) 76.2, (b) 38.1, (c) 19.1, and (d) 9.5 mW cm^{-2} for 1 h, and (e) 9.5 mW cm^{-2} for 2 h. Data are taken from Table S2; see the caption of Table S2 for other reaction conditions.

Table 1 Actual loading amounts of Pd and Au in the samples prepared by the SPD method with various photoirradiation conditions[a]

	Conditions in the SPD process			
Entry	Light intensity (mW cm^{-2})	Irradiation time (h)	Au (wt%)	Pd (wt%)
a	76.2	1	1.09	2.04
b	38.1	1	1.05	1.35
c	19.1	1	1.05	0.81
d	9.5	1	1.08	0.75
e	9.5	2	1.11	0.90

[a] The intended loading amounts for each sample were 1 and 2 wt% for Au and Pd, respectively. The loading amount is determined by XRF. The XRF spectra are shown in Fig. S3.

2 wt% Pd (Table 1, entry a). For the other samples, the Au precursors were fully deposited to form the Au core, but the Pd precursors were partially deposited under the present conditions (Table 1, entries b–d). This indicates that in the SPD process, the Au precursor is more easily photodeposited than the Pd precursor in these conditions and some of the Pd precursors remained in the preparation solution in some conditions and were not deposited.

Thus, an additional experiment was performed with an extended irradiation time with the lowest light intensity in the SPD process (Table 1, entry e). The photoirradiation for 2 h gave a larger loading of Pd, which was almost equivalent to the case of two times SPD light intensity (Table 1, entry e). Note that the loading amount is not two times larger than the case of 1-h irradiation (Table 1, entry d) because the photodeposition rate is proportional to the decreasing concentration of the precursor in the solution. In this sample (Table 1, entry e), all the Au precursors were deposited for the initial 1 h and thus the additional 1-h photoirradiation should deposit only Pd metal on the surface of the Au@Pd core–shell generated at the first 1-h irradiation, meaning that almost pure Pd shell additionally covers on the core–shell structure, *i.e.*, the very surface of the NPs consists of pure Pd layer. This sample exhibited a unique performance in the photocatalytic reaction test (Fig. 2e), showing the higher Y_{C11-d}, S_d and R_d (%) values than the sample prepared with the SPD for 1 h (Fig. 2d), indicating the additional deposited pure Pd shell contribute to the selective deuteration. In addition, another property was clarified when compared with the sample prepared by the SPD light intensity of 19.1 mW cm^{-1} (Fig. 2c), which contain the similar amount of Au and Pd due to the similar number of irradiated photons. Both the samples showed similar Y_{C11-d} but different S_d and R_d (%) values, meaning that the sample prepared with low light intensity for a longer irradiation time can selectively give the deuterated compound. This should be due to the pure Pd surface of the core–shell Au@Pd cocatalyst. The sample prepared by the maximum SPD light intensity, which would have larger amount of the pure Pd surface on the Au@Pd core–shell cocatalyst, exhibited further high activity and selectivity (Fig. 2a). Thus, it is concluded that the concentration gradient core–shell Au@Pd NPs well covered by the pure Pd surface can selectively promote this photocatalytic reaction.

STEM-EDX images (Fig. 3) show that these samples have core–shell structure as expected. The Pd signal became weaker as the light intensity decreased from 76.2 to 9.5 mW cm^{-2} (Fig. S1d and 3d, h, l), corresponding to the decrease in Pd loading (Table 1). In contrast, the Au signal remained relatively constant, suggesting that Au deposition was less sensitive to light intensity in the SPD process. Furthermore, the Au1@Pd2/TiO$_2$ sample prepared under 9.5 mW cm^{-2} for 2 h (Fig. 3p) shows a relatively thicker Pd shell compared with the sample deposited for 1 h under the same intensity (Fig. 3l), indicating that the thicker pure Pd surface promotes this photocatalytic reaction selectivity (Fig. 2e).

Here, leaving aside the bimetallic cocatalyst, the photodeposition of Au NPs was investigated. Results of photocatalytic reaction test with some Au1/TiO$_2$ photocatalyst prepared with different PD light intensity (Fig. 4). The sample prepared at 76.2 mW cm^{-2} exhibited the highest Y_{C11-d}, S_d (%), and R_d (%). During the PD process, the high light intensity gives a larger number of photoexcited electrons on the TiO$_2$ surface and promotes photodeposition of Au NPs at larger numbers of reduction sites on the surface, providing a larger number of small Au NPs. This is supported by the particle size distribution estimated from TEM images of the Au1/TiO$_2$ samples (Fig. S5), showing the representative sizes of NPs were 8, 10, 11, and 12 nm for the samples with decreasing PD light intensity.

Similarly, in the case of the Au1@Pd2/TiO$_2$ samples, a larger number of small Au@Pd core–shell NPs was observed when the sample was prepared by the high SPD light intensity (Fig. S6), showing the representative sizes of NPs were 5, 7, 7, and 8 nm for the samples with decreasing SPD light intensity. The slightly high dispersion of the small NPs in the best sample would be another positive factor of the Au1@Pd2/TiO$_2$ sample prepared with the high light intensity. The color variation of the Au@Pd/TiO$_2$ samples from dark grey to deep purple with decreasing SPD light intensity mentioned above (Fig. S4) can be explained by the dispersion of the core–shell Au@Pd NPs, *i.e.*, dark gray comes from the core–shell Au@Pd NPs consisting of the pure Pd surface and small size of Au core while the deep purple originates from less content of Pd shell and large size of Au core showing LSPR absorption.

Representative sizes of NPs were 8 and 5 nm for the Au1/TiO$_2$ and Au1@Pd2/TiO$_2$ samples, respectively (Fig. S5a and S6a), where the core–shell NPs exhibited smaller size than the Au NPs without Pd shell. This different dispersion is attributed to the difference in the concentration of metal cations in the solution in the PD and SPD process; higher concentration increases the photodeposition rate and gives a larger number of well-dispersed bimetallic nanoparticles, which also enhances photocatalytic activity (Fig. 2).

Sacrificial reagent in the SPD process

The photocatalytic performance of the Au1@Pd2/TiO$_2$ samples prepared with a sacrificial reagent (a hole scavenger) was evaluated, and the results are shown in Fig. 5. These sacrificial reagents can be oxidized by the hole generated on TiO$_2$ photocatalyst in the SPD process. The sample synthesized using
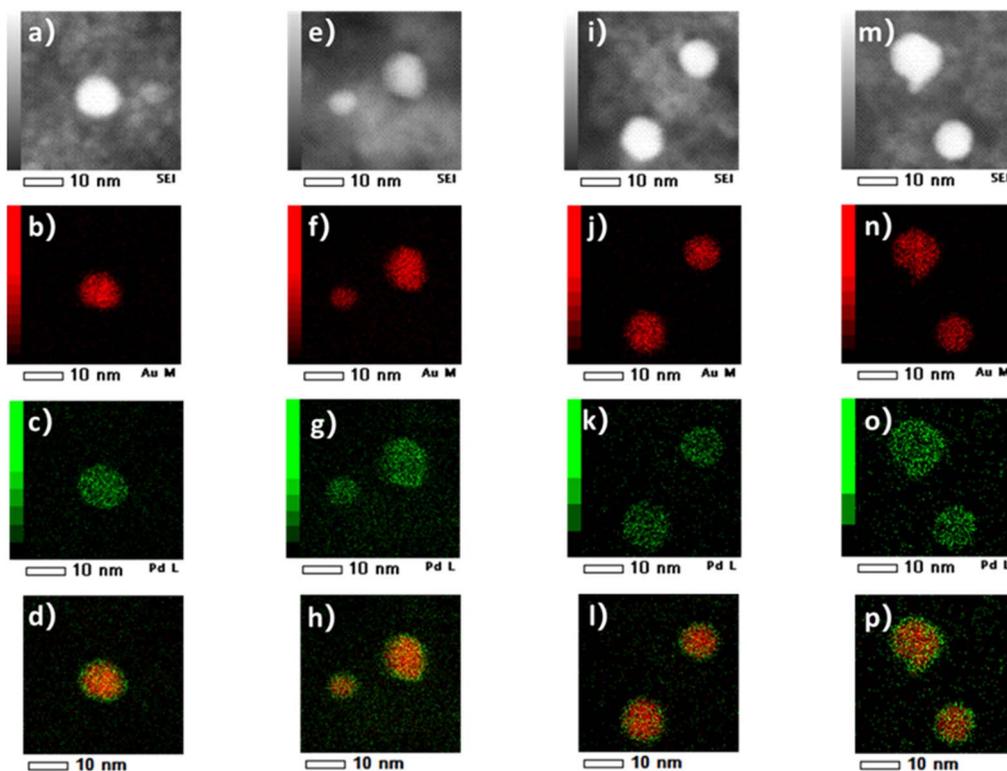
Fig. 3 STEM-EDX elemental mapping of the Au1@Pd2/TiO$_2$ catalysts prepared under different photodeposition light intensities: (a–d) 38.1, (e–h) 19.1, and (i–l) 9.5 mW cm^{-2} for 1 h, and (m–p) 9.5 mW cm^{-2} for 2 h.
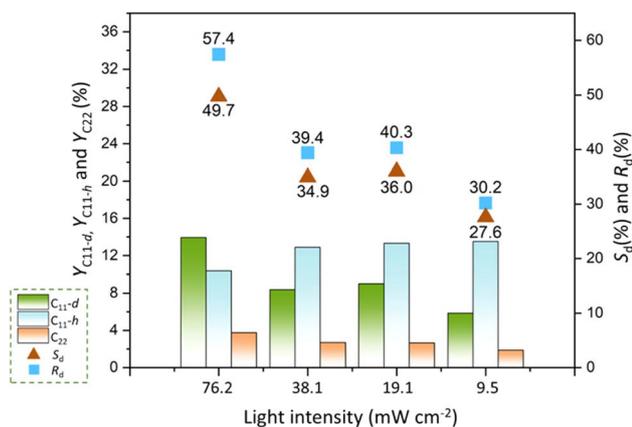

Fig. 4 Results of photocatalytic reaction tests with the Au(1)/TiO$_2$ sample prepared under different light intensity during the photodeposition process. Data are taken from Table S3; see the caption of Table S3 for other reaction conditions.

methanol exhibited the highest C$_{11}$-d Yield and deuterium incorporation efficiency. Those prepared with ethanol and 2-propanol followed, and the catalyst obtained using acetic acid showed the lowest Y_{C11-d} and R_d (%). This trend indicates that various sacrificial reagents during photodeposition much affects the catalytic properties. The actual loading amount of Au and Pd is listed in Table S4 (XRF spectra is shown as Fig. S7). The loading amounts were almost the same as the intended ones, confirming that the use of sacrificial reagent efficiently consumes photogenerated holes to accelerate the

photodeposition of the cocatalyst NPs. Methanol, the most well-known efficient sacrificial reagent, well accelerate the photodeposition, which corresponds to the trend mentioned in the previous section, *i.e.*, efficient reduction of the metal precursors in the SPD process with higher density of the photoexcited electrons, which can be provided by high light intensity or efficient sacrificial reagent such as methanol, leads to the formation of the suitable Au@Pd core–shell nanoparticles covered with a Pd-rich shell surface, resulting in a high yield and selectivity for the production of deuterated undecane.
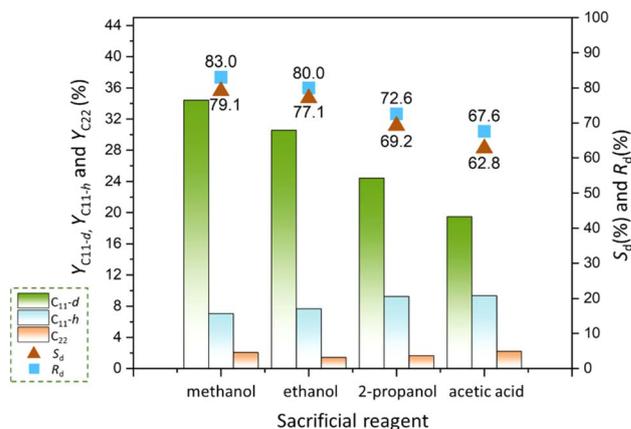

Fig. 5 Results of photocatalytic reaction tests with the Au1@Pd2/TiO$_2$ sample prepared in the presence of different sacrificial reagent during SPD process. Data are taken from Table S4; see the caption of Table S4 for other reaction conditions.

Fig. S8a–d show TEM images of the Au1@Pd2/TiO$_2$ photocatalysts prepared using different sacrificial agents. The particle sizes of the Pd–Au NPs with the highest frequency were in the following order: the sample prepared with methanol (5 nm) < ethanol (7 nm) < 2-propanol (9 nm) < acetic acid (11 nm) (Fig. S8). Among these, the sample prepared with acetic acid exhibited fewer well-defined nanoparticles and a broader particle size distribution. Since XRF analysis indicates nearly the same Pd and Au loading amount across all three samples, the different photoactivity results are also attributed to different NPs sizes and dispersion. In conclusion, methanol proved to be the most effective sacrificial reagent in the current conditions among the tested reagents, including additionally tested ethylene glycol, which gave lower activity than methanol and ethanol (Table S4, entry 5).

Effect of additional Pt deposition

Another series of samples, Au1@Pd2/Ptx/TiO$_2$ (Pt: x wt%) were prepared; Pt NPs were loaded on the TiO$_2$ photocatalyst by the PD method before loading Au1@Pd2 core–shell NPs by the SPD method. The results of photocatalytic reaction of the Au1@Pd2/Ptx/TiO$_2$ are shown in Fig. 6. Notably, the Y_{C11-d} (%), S_d (%) and R_d (%) decreased significantly with the increase of Pt loading amount. Meanwhile, the yield of undecane, Y_{C11-h} (%) grew slightly with the increase in Pt loading. It is noted that these samples exhibited lower activity than the Au1@Pd2/TiO$_2$ photocatalyst.

STEM-EDX images demonstrated the structure of the loaded cocatalyst (Fig. S9). For the sample with low Pt loading (0.01 wt%), Pt NPs are observed to be sparsely dispersed at the same place with the Au–Pd bimetallic particles and the Pd-shell exhibits a slightly irregular morphology (Fig. S9a–e), suggesting that the highly dispersed Pt species of small content did not work as the reductive sites for the successive formation of core–shell Au@Pd NPs. Conversely, when the Pt loading was increased to 1.0 wt% (Fig. S9f–j), significant aggregation of Pt particles was observed, as well as partially covered by Au and Pd. It is important to note that some particles consisted of only Pd and Pt, with no distinguishable Au atoms, which is due to the low loading amount of Au compared with that of Pd. The reason for the lower activity is discussed here. The order of the work functions of the metals[36] is as follows: Au (4.78 eV) > Pd (5.01 eV) > Pt (5.03 eV), corresponding to the Fermi levels of 0.34, 0.57, and 0.59 V vs. SHE. In the Au@Pd/TiO$_2$ system, the photoexcited electrons generated in the TiO$_2$ conduction band (ca. −0.4 V vs. SHE)[37] can transfer to the Au core (0.34 V), which functions as an electron reservoir, and subsequently they can move to Pd shell (0.57 V). This process is considered to promote efficient charge separation and electron migration to the surface of the cocatalyst NPs, where the enriched electron density enhances the reduction reactions on the surface. However, upon the introduction of Pt at the interface between TiO$_2$ and Au@Pd core–shell NPs in the Au@Pd/Pt/TiO$_2$, the electrons are initially captured by Pt center (0.59 V). The electron transfer from Pt to Pd becomes thermodynamically unfavorable, thereby decreasing the electron migration rate at the interface and consequent reduction rate by the electrons. This is consistent with the reduced photocatalytic activity of the ternary Au@Pd/Pt/TiO$_2$ catalyst in comparison to the bimetallic Au@Pd/TiO$_2$ system.

DR UV-vis spectra

The DR UV-vis spectra of the above samples prepared with various conditions, i.e., Au1@Pd2/TiO$_2$, Au1/TiO$_2$ and Au1@Pd2/Ptx/TiO$_2$ samples, are shown in Fig. S10. All the samples exhibited a strong absorption edge around 400 nm corresponding to the bandgap of TiO$_2$.[38] In addition, broad absorption extending into the visible region (400–750 nm) was observed, which includes the absorption band assignable to Pd
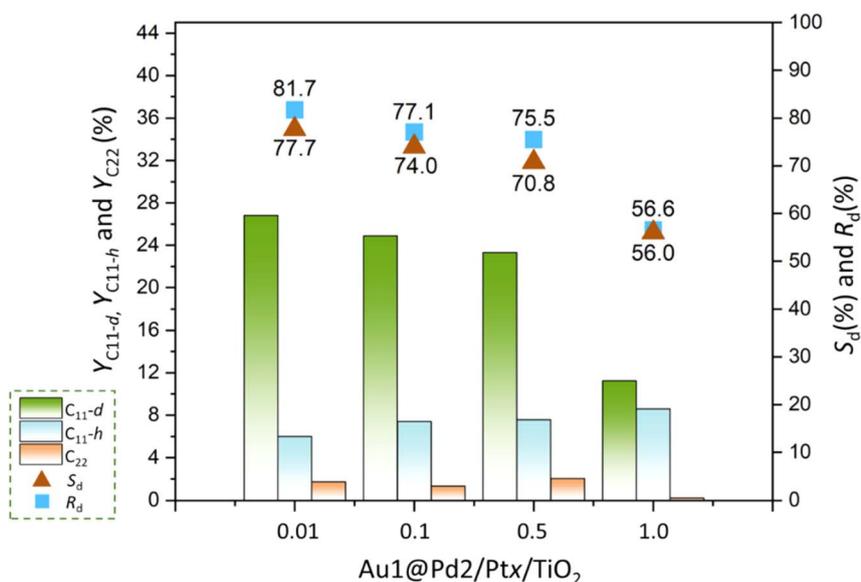

Fig. 6 Results of photocatalytic reaction tests with Au1@Pd2/Ptx/TiO$_2$ sample. Data are taken from Table S5; see the caption of Table S5 for other reaction conditions.

and Au species and the local surface plasmon resonance (LSPR) of Au nanoparticles.

In the spectra of the Au1@Pd2/TiO$_2$ samples prepared under various light intensities in the SPD process (Fig. S10A), the intensity of the visible-light absorption band increased with increasing the SPD light intensity (from 9.5 to 76.2 mW cm^{-2}), suggesting a higher loading or larger particle size of deposited metals under stronger irradiation. This trend agrees with the color change of the samples from light purple to dark grey (Fig. S4), indicating enhanced metal nanoparticle formation. The result confirms that higher SPD light intensity promotes more efficient photoreduction of metal precursors, leading to increased surface coverage of Au or Pd species on TiO$_2$. Interestingly, the spectrum of the sample prepared at 9.5 mW cm^{-2} for 2 h shows similar intensity to that of the samples prepared with the light of 9.5 mW cm^{-2} for 1 h and 19.1 mW cm^{-2} for 1 h. The additional 1-h photoirradiation of low intensity increased Pd shell covering Au NPs, exhibiting the LSPR band to some extent, which did not change the band intensity so much, but much improved the photocatalytic performance. The surface property of the pure Pd shell contributes to the photocatalytic performance.[33]

The DR UV-vis spectra of the Au1/TiO$_2$ samples prepared under different light intensities are shown in Fig. S10B. All the Au/TiO$_2$ samples show a clear LSPR band at around 550–560 nm.[39] The sample prepared under 76.2 mW cm^{-2} exhibits the strongest adsorption, while the weakest one is shown by the sample prepared under the lowest light intensity, 9.5 mW cm^{-2}. However, their differences are not so large. It is indicated that even if the Au NPs exhibiting similar LSPR band, the photocatalytic property of these Au NPs prepared by the PD method is much influenced by the light intensity in the PD process. As mentioned above, the difference in the photocatalytic performance is determined by the particle size of the Au NPs. The size difference is critical for the photocatalytic activity and selectivity, but not for the LSPR band intensity.

The Au1@Pd2/TiO$_2$ catalyst prepared with different hole scavengers exhibited various band structures (Fig. S10C). The best Au1@Pd2/TiO$_2$ photocatalyst prepared with methanol showed a rather clear LSRR band while the other samples showed different band shapes. The use of sacrificial reagent would influence the metal NPs structure and dispersion in various ways. At least, methanol can be recognized as a useful sacrificial reagent.

For the Au@Pd/Ptx/TiO$_2$ samples (Fig. S10D), no clear correlation was observed between the absorption intensity and the Pt loading amount, consistent with the observation of STEM-EDX. The sample with x = 0.5 exhibited the strongest absorption peak, whereas those with x = 0.01 and 1.0 showed comparatively weaker spectra. These irregular trends suggest that the influence of Pt loading on the optical properties and the photocatalyst is not straightforward.

Rational cocatalyst design

It is instructive to examine how light intensity during the simultaneous photodeposition influences the structure and size
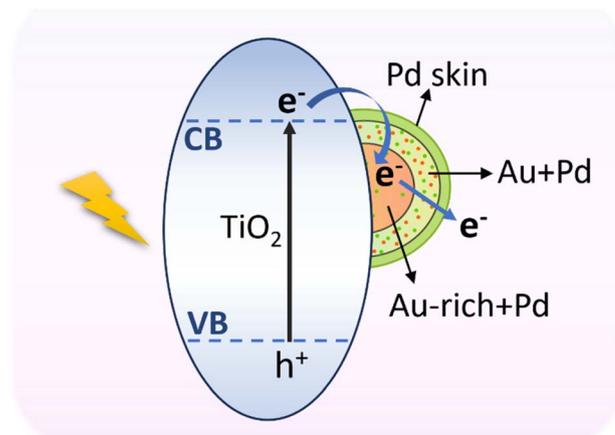
Scheme 1 Schematic diagram describing the electron transfer on the "three-layer" of the core–shell Au@Pd cocatalyst loaded TiO$_2$ photocatalyst.

of Au–Pd NPs loaded onto TiO$_2$. As light intensity increases in the SPD process, the Pd-shell thickens while the Au-core size remains relatively unchanged (with only about 0.7 nm difference). As shown in Scheme 1, Au^{3+} ions are first reduced to form Au-rich center core. Subsequently, Pd^{2+} is reduced and deposited not in distinct layers but intermingled with Au, creating a gradual transition zone between the core and shell. Under stronger illumination, more Pd is deposited, forming a thicker and purer Pd-skin layer covering the Au–Pd particles with a concentration gradient. These structural changes in the Au–Pd NPs strongly influence their photocatalytic performance toward C$_{11}$-d production. As we discussed with Fig. 1, samples with core–shell Au@Pd NPs with a compositional gradient between Au and Pd demonstrate higher activity than those with a distinct, well-defined Au@Pd interface. Furthermore, under low light intensity, extended irradiation time promotes the formation of an additional thicker Pd-rich layer, thereby enhancing deuterium incorporation selectivity.

Structurally, compared with Pd existing alone, the rational design of Au@Pd core–shell structure consisting of (i) Au-rich core, (ii) mixed layer of Au and Pd with concentration gradient, (iii) pure Pd skin, in this sequence, more effectively promotes electron migration toward the Pd surface, giving high electron density at the Pd surface to enhance the reduction reaction of D$^+$ to produce abundant D radicals. These radicals subsequently couple with alkyl radicals to yield the deuterated alkane product (deuterated undecane).

This mechanistic insight highlights how rational control of cocatalyst architecture can guide the design of more efficient photocatalytic systems.

Experimental

Catalyst preparation

Bimetallic cocatalyst preparation. Core–shell Au1@Pd2/TiO$_2$ photocatalysts, where the numbers show the loading (wt%), were prepared by a simultaneous photodeposition (SPD) method using anatase TiO$_2$ (ST-01, Ishihara Sangyo Kaisha, 300

m^2 g^{-1}). Aqueous solutions of $HAuCl_4$ (9.894 g L^{-1}) and $PdCl_2$ (6.411 g L^{-1}) and were used as precursors for cocatalyst. Typically, TiO_2 powder (2 g) was dispersed in deionized water (300 mL) and preirradiated with a 300 W Xe lamp for 30 min. Afterward, 2.0 mL of $HAuCl_4$, 6.2 mL of $PdCl_2$ solutions and 100 mL of methanol as a sacrificial reagent were added. The suspension was stirred for 15 min in the dark and then photoirradiated by a xenon lamp (PE300BUV, 300 W) for 1 h unless otherwise specified. The product was filtered, washed thoroughly with water (>500 mL), and dried at 353 K for 24 h to yield Au1@Pd2/TiO_2 sample. The effect of photodeposition conditions was examined by varying light intensity and sacrificial reagents (methanol, ethanol, 2-propanol, acetic acid, and ethylene glycol).

For step-wise photodeposition, 1 wt% Au was first deposited onto TiO_2, followed by deposition of 2 wt% Pd after drying, yielding a Pd2/Au1/TiO_2 sample, and the opposite sequence gave a Au1/Pd2/TiO_2 sample. A hybrid sample, Pd2(PD)/Au1(CR)/TiO_2, was also prepared by combining chemical reduction (CR) and PD. In the CR process, TiO_2 (2 g) was suspended in 300 mL water containing 2 mL $HAuCl_4$ and stirred at 353 K. Then, 1 mL NaH_2PO_2 as a reductant was added dropwise slowly in 10 min, and the mixture was stirred for 30 min before filtration, washing, and drying.

Preparation of monometallic catalysts. Au1/TiO_2 was prepared using the photodeposition method similar to Au@Pd/TiO_2. 2.0 g of TiO_2 powder was dispersed in 300 mL of ion-exchanged water and irradiated with a xenon lamp (PE300BUV, 300 W) for 30 min under magnetic stirring. Subsequently, 100 mL of methanol and 2 mL of the $HAuCl_4$ solution were added to the suspension. The mixture was stirred for 15 min without irradiation, followed by stirring for 1 h under light irradiation. After irradiation, the suspension was filtered and washed with over 500 mL of deionized water. The wet residue was dried in an electric oven at 353 K for 24 h.

Preparation of trimetallic catalysts. For comparison, Au@Pd/Ptx/TiO_2 samples were also prepared by a modified SPD method. Ptx/TiO_2 was first prepared with x wt% Pt by the PD method, followed by loading Pd and Au with the SPD method to form Au@Pd on the Ptx/TiO_2 under the same conditions.

Catalyst characterization

Particle distribution was observed by using transmission electron microscopy (TEM) on a JEM-2200FS instrument (JEOL). Elemental mapping was performed using scanning transmission electron microscopy with energy-dispersive X-ray spectroscopy (STEM-EDX) on a JEM-ARM200F instrument (JEOL). Diffuse-reflectance (DR) UV-vis spectra was measured with a V-770 (JASCO), where a $BaSO_4$ plate was used as a reference. The X-ray fluorescence (XRF) analysis was carried out in an EDX-8000 instrument (Shimadzu), using 50 kV and 1 mA to determine the loading amount of the cocatalyst metals.

Photocatalytic reaction test

The photocatalytic deuteration of lauric acid (LA) was carried out in a sealed 20 mL quartz tube under xenon lamp irradiation

(PE300BUV, 300 W, λ > 360 nm, 41 mW cm^{-2} when measured at 360 ± 20 nm), following the procedure reported previously.[32] Prior to the reaction, 50 mg of photocatalyst was preheated at 450 K under Ar flow (15 mL min^{-1}) for 30 min and pre-irradiated for 15 min to remove adsorbed species. The reaction mixture contained 50 μmol of LA, 60 vol% D_2O, and 40 vol% CH_3CN (5 mL total). After Ar purging, the suspension was photoirradiated for 180 min at 298 K with magnetically stirring. Gaseous products were analysed by GC (Shimadzu GC-8A, TCD), while liquid products were quantified using GC-MS (Shimadzu QP-2020) and GC-FID (Shimadzu GC-2014) with n-decane as an internal standard.

Conclusions

In summary, it has been demonstrated that controlling the structure and function of the cocatalyst in Au@Pd/TiO_2 photocatalyst with desired photodeposition parameters provides a high product yield and selectivity in the photocatalytic synthesis of deuterated alkane from lauric acid and heavy water through decarboxylation. Systematic studies have revealed that light intensity, deposition time, and the selection of sacrificial reagents significantly influence the formation of the Au@Pd core–shell structure. The optimized catalyst exhibits a core–shell structure comprising an Au-rich core, an Au–Pd mixed transition layer, and a Pd-rich surface shell. The layered structure consisting of Au and Pd establishes an internal potential gradient that facilitates directed electron transfer from TiO_2 to the Pd surface. This process enhances charge separation and promotes the generation of active deuterated radicals, improving both selectivity for deuteration reaction and overall yield. The present findings highlight the critical role of rational design of bimetallic cocatalyst on photocatalysts, thus providing valuable guidance for the development of efficient and sustainable photocatalytic deuteration systems.

Author contributions

H. H.: investigation, methodology, and writing – original draft; H. Y.: conceptualization, supervision, writing – review & editing, and funding acquisition.

Conflicts of interest

There are no conflicts to declare.

Data availability

The authors confirm that the data supporting the findings of this study are available within the manuscript and its supplementary information (SI). Raw data that support the findings of this study are available from the corresponding author, upon reasonable request. Supplementary information: STEM-EXD images and line analysis, results of photocatalytic reaction tests, XRF spectra, photographs of the samples, TEM images, particle size distributions, DR UV-vis spectra. See DOI: https://doi.org/10.1039/d5ra08602g.

Acknowledgements

References

1 J. D. Dabbs, C. C. Taylor, M. S. Holdren, S. E. Brewster, B. T. Quillin, A. Q. Meng, D. A. Dickie, B. H. Pate and W. D. Harman, *Nat. Commun.*, 2024, **15**, 8473.

2 H. Yang, L. Tian, A. Grirrane, A. García-Baldoví, J. Hu, G. Sastre, C. Hu and H. García, *ACS Catal.*, 2023, **13**, 15143–15154.

3 G. Prakash, N. Paul, G. A. Oliver, D. B. Werz and D. Maiti, *Chem. Soc. Rev.*, 2022, **51**, 3123–3163.

4 L. Wang, X. Xing, X. Zeng, S. R. E. Jackson, T. TeSlaa, O. Al-Dalahmah, L. Z. Samarah, K. Goodwin, L. Yang, M. R. McReynolds, X. Li, J. J. Wolff, J. D. Rabinowitz and S. M. Davidson, *Nat. Methods*, 2022, **19**, 223–230.

5 H. M. De Feyter and R. A. de Graaf, *J. Magn. Reson.*, 2021, **326**, 106932.

6 A. Matsugi, K. Suma and A. Miyoshi, *Phys. Chem. Chem. Phys.*, 2011, **13**, 4022–4031.

7 M. Urrestizala, J. Azkurreta, N. Alegría and I. Peñalva, *Fusion Eng. Des.*, 2023, **194**, 113915.

8 S. H. DeWitt and B. E. Maryanoff, *Biochemistry*, 2018, **57**, 472–473.

9 W. Ou, C. Qiu and C. Su, *Chin. J. Catal.*, 2022, **43**, 956–970.

10 J. Martin, J. Eyselein, S. Grams and S. Harder, *ACS Catal.*, 2020, **10**, 7792–7799.

11 A. Burhop, R. Weck, J. Atzrodt and V. Derdau, *Eur. J. Org. Chem.*, 2017, **2017**, 1418–1424.

12 Y. Dong, Y. Su, L. Du, R. Wang, L. Zhang, D. Zhao and W. Xie, *ACS Nano*, 2019, **13**, 10754–10760.

13 A. Di Giuseppe, R. Castarlenas and L. A. Oro, *C. R. Chim.*, 2015, **18**, 713–741.

14 N. Zhu, M. Su, W. M. Wan, Y. Li and H. Bao, *Org. Lett.*, 2020, **22**, 991–996.

15 N. Li, Y. Li, X. Wu, C. Zhu and J. Xie, *Chem. Soc. Rev.*, 2022, **51**, 6291–6306.

16 A. Tortajada and E. Hevia, *Catal. Sci. Technol.*, 2023, **13**, 4919–4925.

17 M. Valero, A. Mishra, J. Blass, R. Weck and V. Derdau, *ChemistryOpen*, 2019, **8**, 1183–1189.

18 S. Kopf, F. Bourriquen, W. Li, H. Neumann, K. Junge and M. Beller, *Chem. Rev.*, 2022, **122**, 6634–6718.

19 J. Atzrodt, V. Derdau, W. J. Kerr and M. Reid, *Angew. Chem., Int. Ed.*, 2018, **57**, 3022–3047.

20 J. Atzrodt, V. Derdau, T. Fey and J. Zimmermann, *Angew. Chem., Int. Ed.*, 2007, **46**, 7744–7765.

21 W. N. Palmer and P. J. Chirik, *ACS Catal.*, 2017, **7**, 5674–5678.

22 Y. Chang, A. Yesilcimen, M. Cao, Y. Zhang, B. Zhang, J. Z. Chan and M. Wasa, *J. Am. Chem. Soc.*, 2019, **141**, 14570–14575.

23 C. Zhang, Z. Shen, L. Tian and L. Chen, *J. Labelled Compd. Radiopharm.*, 2012, **55**, 401–405.

24 G. Srinivas, V. K. P. Unny, K. Mukkanti and B. M. Choudary, *J. Labelled Compd. Radiopharm.*, 2013, **56**, 325–329.

25 R. Ferrando, J. Jellinek and R. L. Johnston, *Chem. Rev.*, 2008, **108**, 845–910.

26 M. Luo and S. Guo, *Nat. Rev. Mater.*, 2017, **2**, 1–13.

27 A. K. Singh and Q. Xu, *ChemCatChem*, 2013, **5**, 652–676.

28 X. Zhang, Z. Sun, R. Jin, C. Zhu, C. Zhao, Y. Lin, Q. Guan, L. Cao, H. Wang, S. Li, H. Yu, X. Liu, L. Wang, S. Wei, W. X. Li and J. Lu, *Nat. Commun.*, 2023, **14**, 530.

29 J. E. S. van der Hoeven, J. Jelic, L. A. Olthof, G. Totarella, R. J. A. van Dijk-Moes, J. M. Krafft, C. Louis, F. Studt, A. van Blaaderen and P. E. de Jongh, *Nat. Mater.*, 2021, **20**, 1216–1220.

30 T. A. G. Silva, E. Teixeira-Neto, N. López and L. M. Rossi, *Sci. Rep.*, 2014, **4**, 5766.

31 A. M. Henning, J. Watt, P. J. Miedziak, S. Cheong, M. Santonastaso, M. Song, Y. Takeda, A. I. Kirkland, S. H. Taylor and R. D. Tilley, *Angew. Chem., Int. Ed.*, 2013, **52**, 1477–1480.

32 H. Huang, Z. Lin, A. Yamamoto, Y. P. Bhoi, K. Zou, S. Furukawa, K. Fujita, G. Lee, J. Kumagai and H. Yoshida, *Catal. Sci. Technol.*, 2025, **15**, 4637–4648.

33 H. Huang, A. Yamamoto, R. Sugiyama, A. Tanaka, H. Kominami and H. Yoshida, *Catal. Today*, 2026, **461**, 115520.

34 S. G. Bratsch, *J. Phys. Chem. Ref. Data*, 1989, **18**, 1–21.

35 P. Atkins and d. J. Paula, *Elements of Physical Chemistry*, Oxford University Press, Great Britain, 2009.

36 S. Trasatti, *J. Electroanal. Chem. Interfacial Electrochem.*, 1972, **39**, 163–184.

37 J. ichi Fujisawa, T. Eda and M. Hanaya, *Chem. Phys. Lett.*, 2017, **685**, 23–26.

38 A. K. Singh and Q. Xu, *ChemCatChem*, 2013, **5**, 652–676.

39 A. Naldoni, F. Riboni, M. Marelli, F. Bossola, G. Ulisse, A. Di Carlo, I. Píš, S. Nappini, M. Malvestuto, M. V. Dozzi, R. Psaro, E. Selli and V. Dal Santo, *Catal. Sci. Technol.*, 2016, **6**, 3220–3229.